

# Structural and Magnetic Properties of $\text{Mn}_{1-x}\text{Zn}_x\text{Fe}_2\text{O}_4$ Ferrite Nanoparticles

C. Murugesan<sup>1</sup> · G. Chandrasekaran<sup>1</sup>

Received: 6 April 2016 / Accepted: 24 June 2016 / Published online: 20 July 2016  
© Springer Science+Business Media New York 2016

**Abstract** In this work, solid solutions of  $\text{Mn}_{1-x}\text{Zn}_x\text{Fe}_2\text{O}_4$  (where  $x = 0.0, 0.2, 0.4, 0.6, 0.8,$  and  $1.0$ ) ferrite nanoparticles were synthesized using the novel combustion method. A powder X-ray diffraction study confirms the formation of spinel-structured  $\text{Mn}_{1-x}\text{Zn}_x\text{Fe}_2\text{O}_4$ . Unusual increases in the lattice constant were observed from 8.358 to 8.435 Å for Zn substitution. Raman spectra show the change in local environment of tetrahedral and octahedral symmetry. Field emission scanning electron microscopy images show that the prepared samples are nanosized and there is not much difference observed in surface morphology. A magnetic study reveals that the prepared samples exhibit superparamagnetic properties with negligible coercivity and the saturation magnetizations initially increase from 31.12 emu  $\text{g}^{-1}$  ( $x = 0$ ) to 35.48 emu  $\text{g}^{-1}$  ( $x = 0.2$ ) and then decrease for further Zn substitution at 300 K. The zero-field-cooled and field-cooled magnetization studies confirm the superparamagnetic nature of prepared samples, and the observed blocking temperature decreases from 146.05 to 32.3 K. At 20 K, the measured hysteresis loop shows the coercivity and it gradually decreases from 810 to 152 Oe. The obtained results suggest that the prepared superparamagnetic  $\text{Mn}_{1-x}\text{Zn}_x\text{Fe}_2\text{O}_4$  ferrite nanoparticles are a promising candidate material for biomedical applications.

**Keywords** Spinel ferrite · Auto combustion · Superparamagnetic · Coercivity · Saturation magnetization · Blocking temperature · Anisotropy

## 1 Introduction

Oxide-based magnetic materials are technologically important materials, due to their magnetic properties combined with high electrical resistivity and good thermal stability [1, 2]. In particular, spinel ferrites ( $\text{MFe}_2\text{O}_4$ ,  $\text{M} = \text{Co}, \text{Ni}, \text{Mn}, \text{Mg}, \text{Zn},$  etc) are widely used in electronic and medical applications due to their low cost and excellent performance [3–5]. Among them, MnZn is an important material having excellent electromagnetic properties such as high permeability, saturation magnetization and electrical resistivity [6, 7]. The unique functionality of MnZn ferrites makes it a promising material for inductors, transformer cores, antenna rods, deflection yokes, choke coils, recording heads and electromagnetic interference devices [8–13]. In the past few decades with the advent of nanotechnology there has been renewed interest on the synthesis of spinel ferrite nanoparticles with the potential application in the field of nanostructured materials. As an important soft magnetic material, nanosized Mn–Zn ferrite finds applications in photocatalysts [14], hyperthermia [15] and ferrofluids [16]. These abovementioned applications particularly require only smaller-size nanoparticles. The properties of prepared spinel ferrite are significantly influenced by its synthesizing method [17]. It is well known that MnZn ferrites were previously prepared using the conventional solidstate reaction method. The particles obtained by such a high temperature method are significantly larger and

✉ C. Murugesan  
murugesanscience@gmail.com

<sup>1</sup> Department of Physics, School of Physical, Chemical and Applied Sciences, Pondicherry University, Kalapet, Puducherry 605014, India

not in nanosize [18]. In recent decades extensive research activities have been focused on the preparation of MnZn ferrite nanoparticles by using several non-conventional synthesis methods such as hydrothermal precipitation [19], microemulsion reaction [20], sol–gel auto combustion [21], reverse micelles [22], co-precipitation [23], etc. In the present work a nonconventional synthesis method, known as the novel combustion method, was used for the preparation of nanosized  $\text{Mn}_{1-x}\text{Zn}_x\text{Fe}_2\text{O}_4$  ferrites. The novel combustion method is a simplified form of sol–gel combustion method. Its novelty lies in the direct mixing of reactants and the fuel compared with the sol–gel combustion method. Since the hygroscopic nature of metal nitrates tends to form a slurry mixture, we have not used any solvent to dissolve the nitrates and citric acid. Furthermore, we have not changed any pH value to change the reaction kinetics which is usually used in the sol–gel combustion method [10]. This method may be a good candidate for synthesis of a large quantity of homogeneous ferrite powders due to simplicity in its preparation process as well as cost-effectiveness, a short preparation time, a much lower processing temperature and easy reproducibility. It is of further interest to replace a magnetic  $\text{Mn}^{2+}$  cation by a non-magnetic  $\text{Zn}^{2+}$  cation for an understanding of the structural and magnetic properties. The possible mechanisms contributing to these observed results have been discussed in detail.

## 2 Experimental

### 2.1 Synthesis

Solid solutions of  $\text{Mn}_{1-x}\text{Zn}_x\text{Fe}_2\text{O}_4$  (where  $x = 0.0, 0.2, 0.4, 0.6, 0.8,$  and  $1.0$ ) ferrite nanoparticles were synthesized using the novel combustion method. AR-grade manganese nitrate, zinc nitrate, ferric nitrate, and citric acid were used as reactants. Organic fuel citric acid provides a platform for the redox reactions to occur between the reactants during the course of the auto combustion reaction. The required amount of reactants was weighed and taken in a glass beaker. The hygroscopic nature of metal nitrates tends to form a slurry mixture when they are mixed using a magnetic stirrer for 30 min. The obtained mixture dehydrated by heating at  $75^\circ\text{C}$  with continuous stirring on a hot plate to obtain a dried gel. Then, the dried gel heated on a hot plate until it got self-ignited. The self-ignited final product was ground well and calcined at  $450^\circ\text{C}$  for 1 h then used for further characterization.

### 2.2 Characterization

The powder X-ray diffraction (PXR) pattern of all the samples was obtained using a X-ray powder diffractometer

(RIGAKU, Ultima IV) employing  $\text{Cu-K}\alpha$  (wavelength  $1.5406\text{ \AA}$ ) in the  $2\theta$  range of  $20\text{--}80^\circ$  at the step size of  $0.02^\circ$ . The instrument operated at 40 kV and 30 mA. Raman spectra were recorded using a LASER Raman spectrophotometer (Renishaw inVia Reflex) equipped with a CCD camera using Ar ion laser (488 nm) over the range of  $150\text{--}900\text{ cm}^{-1}$ . The surface morphology and elemental composition of all the samples were examined using a field emission scanning electron microscope (FE-SEM, Carl Zeiss SUPRA 55) equipped with energy-dispersive spectroscopy (EDS). The magnetic properties were investigated using a vibrating sample magnetometer (Lakeshore-USA, Model 7407).

## 3 Results and Discussion

### 3.1 Powder X-ray Diffraction Analysis

The PXR patterns of  $\text{Mn}_{1-x}\text{Zn}_x\text{Fe}_2\text{O}_4$  ferrite nanoparticles are shown in Fig. 1. The broad peaks of PXR patterns indicate that the prepared ferrites are smaller in size. Analysis of the diffraction patterns shows the reflection planes (2 2 0), (3 1 1), (2 2 2), (4 0 0), (4 2 2), (5 1 1), (4 4 0), (6 2 0), (5 3 3), and (6 2 2). These reflection planes confirm that the prepared samples are polycrystalline in nature with a cubic spinel structure. The reflection planes of manganese ferrite and zinc ferrite are indexed to JCPDS ( $\text{MnFe}_2\text{O}_4$ -NO: 89-2807,  $\text{ZnFe}_2\text{O}_4$ -NO: 89-4926). It is noticed that there is no

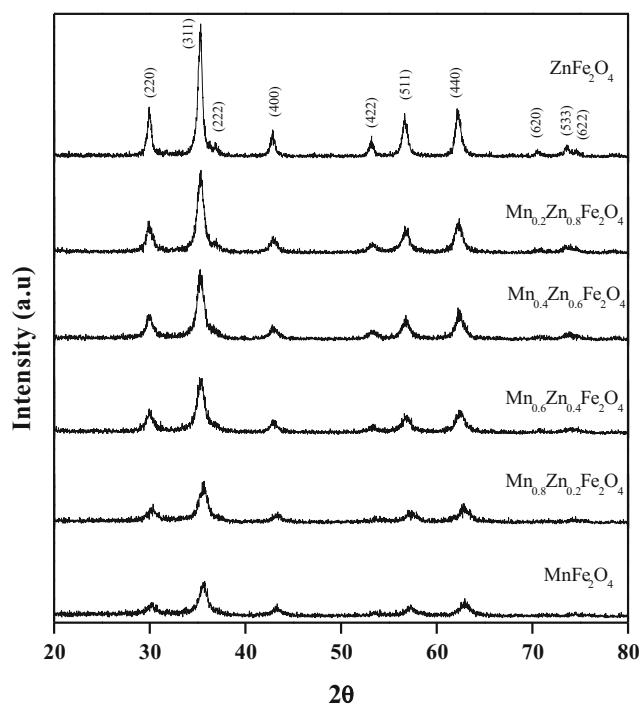


Fig. 1 PXR patterns of  $\text{Mn}_{1-x}\text{Zn}_x\text{Fe}_2\text{O}_4$  ferrite nanoparticles

additional reflection plane corresponding to any secondary phase in pure MnFe<sub>2</sub>O<sub>4</sub>. Furthermore, the PXRD analysis indicates that the Zn<sup>2+</sup> substitution did not result in any new secondary phases. The crystallite size (*D*) was calculated for a high-intensity (3 1 1) plane using Scherrer’s formula [24].

$$D = K\lambda/\beta \cos \theta, \tag{1}$$

where *K* is the Debye–Scherrer constant,  $\lambda$  is the X-ray wavelength,  $\beta$  is the full width at half maximum, and  $\theta$  is the Bragg angle. The calculated values of crystallite size are given in Table 1. It is noticed that the size of pure MnFe<sub>2</sub>O<sub>4</sub> is 8.5 nm and for initial substitution of Zn ( $x = 0.2$ ) we have not observed significant change in size. For further substitution ( $x = 0.4$  to  $x = 0.8$ ), the size of the crystallites increases slowly and reaches a maximum value of 19.6 nm for pure ZnFe<sub>2</sub>O<sub>4</sub>. This indicates that the ratio of Mn and Zn might have an important impact on the number of nuclei formed during the reaction which can determine the crystallite size of Mn<sub>1-x</sub>Zn<sub>x</sub>Fe<sub>2</sub>O<sub>4</sub> [16]. The unit cell parameter of spinel-structured Mn<sub>1-x</sub>Zn<sub>x</sub>Fe<sub>2</sub>O<sub>4</sub> might be a direct evidence for the substitution of Zn, and the value of the lattice constant is determined using the relation [24]

$$a = (\lambda/2)^* \sqrt{(h^2 + k^2 + l^2)/\sin^2 \theta}, \tag{2}$$

where *a* is the lattice constant;  $\lambda$  is the wavelength; *h*, *k*, and *l* are Miller indices; and  $\theta$  is the Bragg angle. The calculated values of the lattice constant of Mn<sub>1-x</sub>Zn<sub>x</sub>Fe<sub>2</sub>O<sub>4</sub> nanoparticles are given in Table 1. The value of the lattice constant of MnFe<sub>2</sub>O<sub>4</sub> and ZnFe<sub>2</sub>O<sub>4</sub> nanoparticles is similar to that of literature reports [25, 26]. We have noticed that the substitution of Zn<sup>2+</sup> considerably influences the lattice constant of MnFe<sub>2</sub>O<sub>4</sub>. Since the ionic radius of Zn<sup>2+</sup> (0.74 Å) is lower than that of Mn<sup>2+</sup> (0.82 Å), a decrease in the lattice constant for Zn<sup>2+</sup> substitution is expected as reported in literature [27]. We have noticed that the value of the lattice constant is increasing for Zn<sup>2+</sup>-doped samples. The lattice constant of bulk MnFe<sub>2</sub>O<sub>4</sub> is 8.51 Å and that of ZnFe<sub>2</sub>O<sub>4</sub> is 8.44 Å, respectively [3]. It is noticed from Table 1 that there

is a contraction in the lattice constant of MnFe<sub>2</sub>O<sub>4</sub> (8.358 Å) compared with bulk MnFe<sub>2</sub>O<sub>4</sub> [28]. The decrease in the lattice constant of nanosized MnFe<sub>2</sub>O<sub>4</sub> could be attributed to the presence of Mn<sup>3+</sup> (0.645 Å) ions in octahedral sites with a smaller ionic radius compared with Mn<sup>2+</sup> (0.82 Å) [27, 29, 30]. It is noticed that the lattice constant of nanosized ZnFe<sub>2</sub>O<sub>4</sub> (8.435 Å) is higher than that of MnFe<sub>2</sub>O<sub>4</sub> (8.358 Å); hence, the substitution of Zn<sup>2+</sup> increases the lattice constant.

### 3.2 Raman Spectra Analysis

Raman spectroscopy is used to find out the microscopic vibrations caused by slight structural distortion due to its good sensitivity to the coordination environments of cations, cation distributions, and oxidation states [31]. We used to obtain structural information of Mn<sub>1-x</sub>Zn<sub>x</sub>Fe<sub>2</sub>O<sub>4</sub> ferrite nanoparticles due to the presence of different cations (such as Mn<sup>2+</sup>, Mn<sup>3+</sup>, Zn<sup>2+</sup>, Fe<sup>2+</sup>, and Fe<sup>3+</sup>) and they occupy different sites in spinel matrix. The molecular formula of spinel ferrite is M<sup>2+</sup>Fe<sub>2</sub><sup>3+</sup>O<sub>4</sub><sup>-4</sup> (M<sup>2+</sup> = Co, Zn, Mn, Mg, or other divalent cations), in which the lattice of O<sup>2-</sup> ions forms tetrahedral (A sites) and octahedral (B sites) local symmetry. Depending upon the divalent and trivalent metal cation arrangements, the spinel structure is classified into three types such as normal, inverse, and mixed spinel, respectively. In normal spinel, the divalent M<sup>2+</sup> ions occupy only A sites, and trivalent Fe<sup>3+</sup> ions occupy only B sites. In inverse spinel, half of the B sites occupy divalent M<sup>2+</sup> and Fe<sup>3+</sup> ions occupy the rest of the B sites and all A sites. In case of mixed spinel, divalent M<sup>2+</sup> occupies both A and B sites, respectively [6]. Raman spectra of all the samples are recorded at room temperature and shown in Fig. 2a–f. The obtained Raman spectra have been deconvoluted into individual Lorentzian peaks for more accurate analysis. The obtained positions of the vibrational bands are given in Table 2. It is clearly seen that though the PXRD patterns of all the samples are similar to each other, the Raman spectra of all the samples are not. It is predicted from the group theory analysis that the spinel structure with the Fd3m space group has 39 normal modes

**Table 1** The crystallite size (*D*), lattice constant obtained from PXRD, and the position of Raman modes of Mn<sub>1-x</sub>Zn<sub>x</sub>Fe<sub>2</sub>O<sub>4</sub> ferrite nanoparticles

Sample	<i>D</i> (nm)	<i>a</i> (Å)	<i>T</i> <sub>2g</sub>	<i>E</i> <sub>g</sub>	<i>E</i> <sub>g</sub>	<i>T</i> <sub>2g</sub>	<i>T</i> <sub>2g</sub>	<i>T</i> <sub>2g</sub>	<i>A</i> <sub>1g</sub>	<i>A</i> <sub>1g</sub>	<i>A</i> <sub>1g</sub>
MnFe <sub>2</sub> O <sub>4</sub>	8.5	8.358	220.6	277.0	–	–	370.9	507.4	593.0	638.7	–
Mn <sub>0.8</sub> Zn <sub>0.2</sub> Fe <sub>2</sub> O <sub>4</sub>	8.2	8.362	220.6	277.0	–	–	370.9	507.4	594.3	640.0	–
Mn <sub>0.6</sub> Zn <sub>0.4</sub> Fe <sub>2</sub> O <sub>4</sub>	9.4	8.419	217.7	275.3	–	–	386.5	490.8	591.3	645.7	–
Mn <sub>0.4</sub> Zn <sub>0.6</sub> Fe <sub>2</sub> O <sub>4</sub>	10.5	8.427	217.8	279.0	347.9	–	–	504.1	596.2	659.9	–
Mn <sub>0.2</sub> Zn <sub>0.8</sub> Fe <sub>2</sub> O <sub>4</sub>	11.5	8.429	174.4	–	339.8	497.1	–	–	622.3	652.7	682.1
ZnFe <sub>2</sub> O <sub>4</sub>	19.6	8.435	174.9	–	340.3	491.0	–	–	–	652.7	688.6

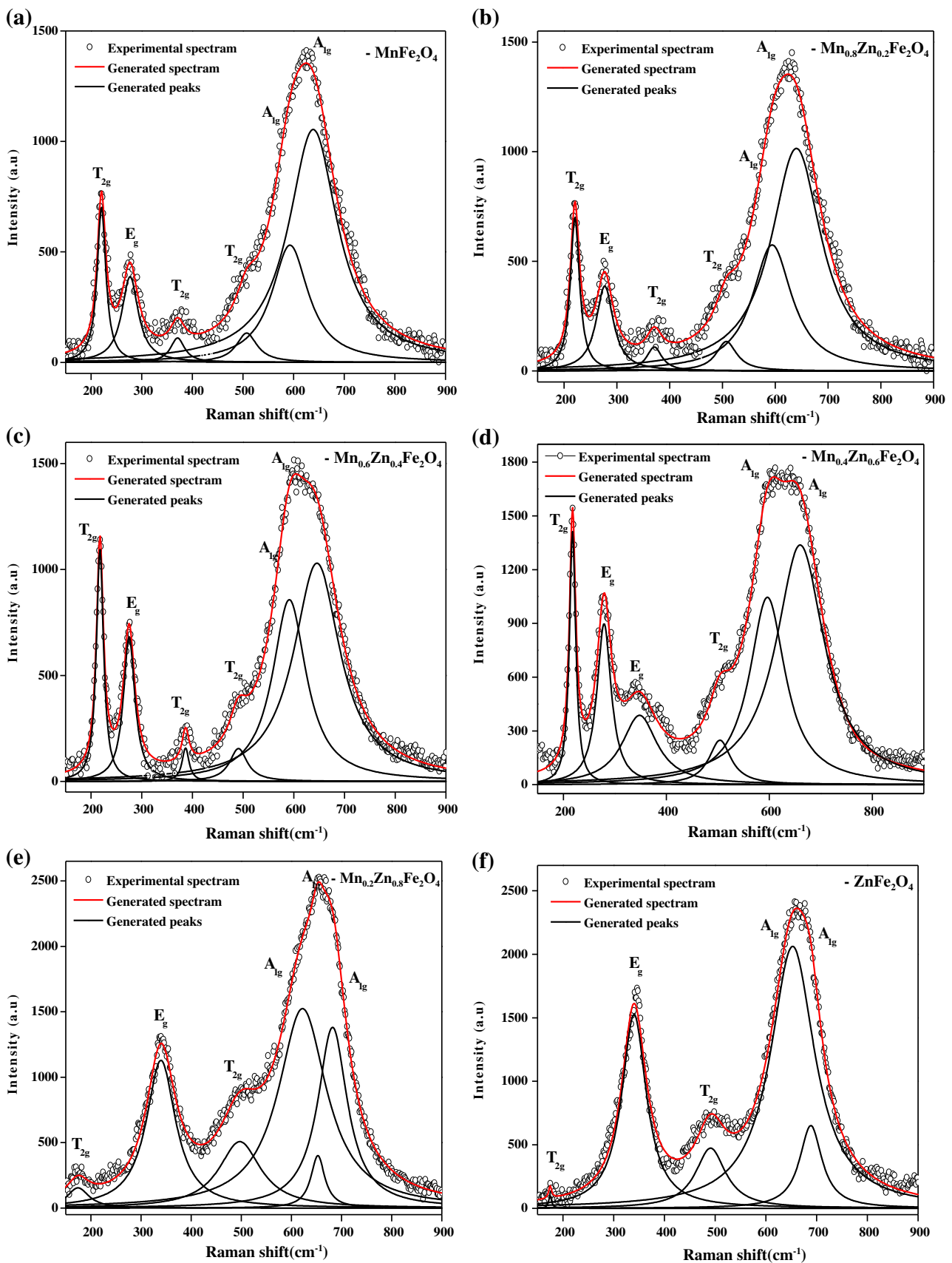


**Fig. 2** a–f The Raman spectra of  $\text{Mn}_{1-x}\text{Zn}_x\text{Fe}_2\text{O}_4$  ferrite nanoparticles



**Table 2** The magnetic parameters of  $Mn_{1-x}Zn_xFe_2O_4$  nanoparticles obtained from the hysteresis curves at 20 and 300 K: the saturation magnetization ( $M_s$ ), coercive field ( $H_c$ ), remanent magnetization ( $M_r$ ), and blocking temperature ( $T_B$ )

Samples	20 K			$M_s$ (emu/g) at 300 K	$T_B$ (K)
	$H_c$ (Oe)	$M_r$ (emu/g)	$M_s$ (emu/g)		
$MnFe_2O_4$	810	15.8	39.16	31.12	146.05
$Mn_{0.8}Zn_{0.2}Fe_2O_4$	468	13.1	44.64	35.48	125.73
$Mn_{0.6}Zn_{0.4}Fe_2O_4$	452	7.5	32.87	22.10	75.80
$Mn_{0.4}Zn_{0.6}Fe_2O_4$	423	7	29.37	13.94	65.65
$Mn_{0.2}Zn_{0.8}Fe_2O_4$	319	4.3	28.69	10.52	45.23
$ZnFe_2O_4$	152	1.5	24.51	9.91	32.3

**Fig. 3** FE-SEM images of  $Mn_{1-x}Zn_xFe_2O_4$  ferrite nanoparticles

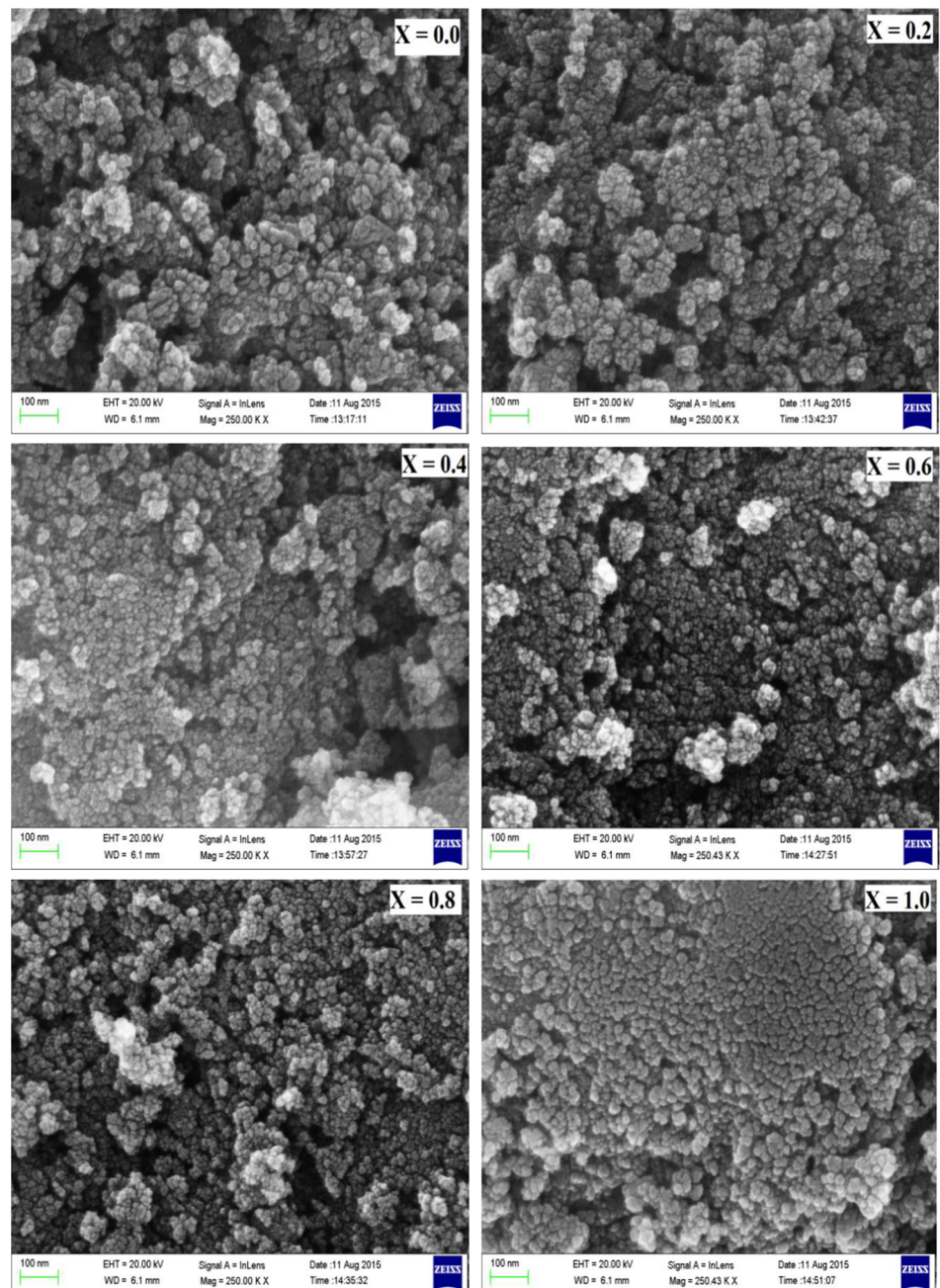
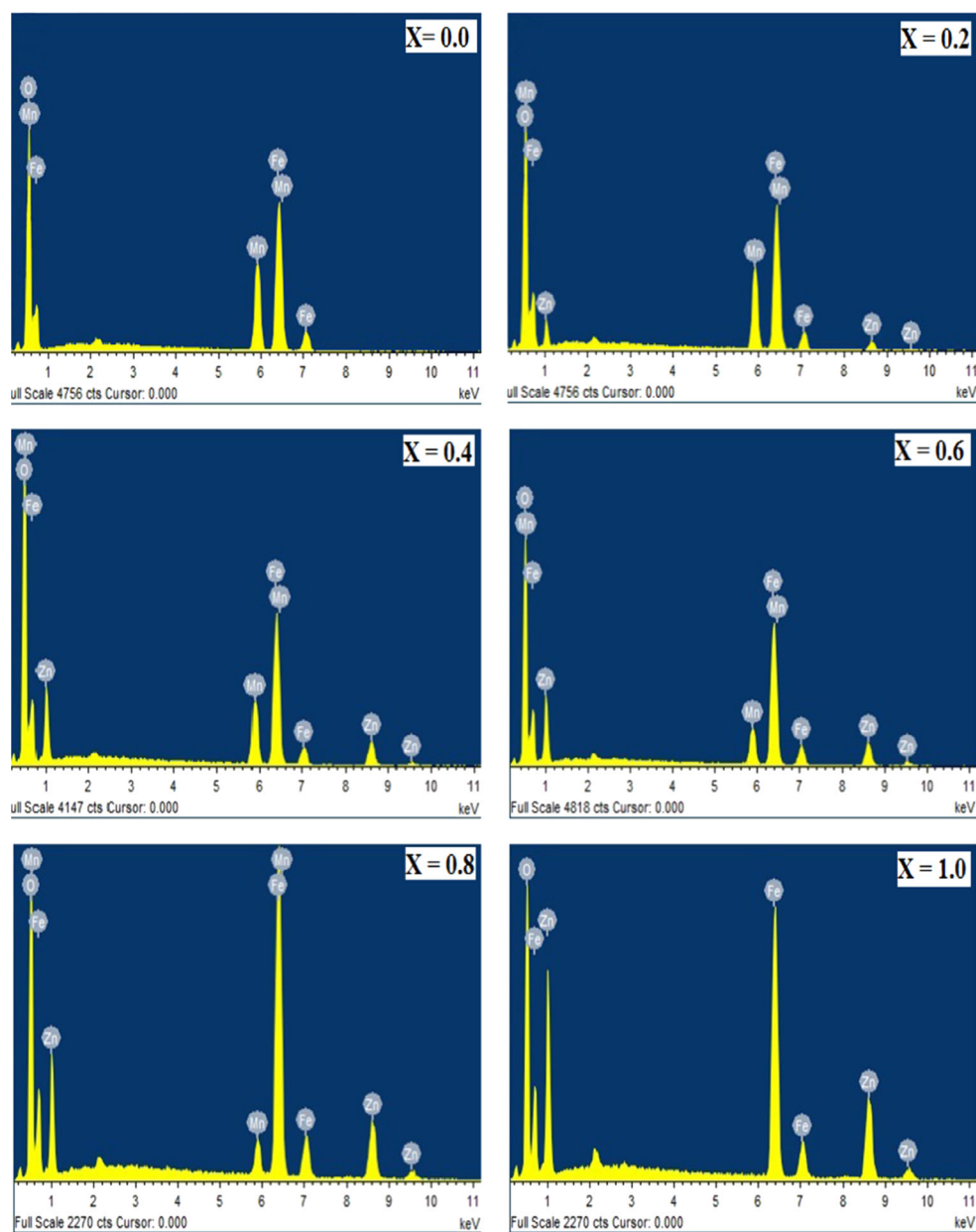


**Fig. 4** EDS spectra of  $\text{Mn}_{1-x}\text{Zn}_x\text{Fe}_2\text{O}_4$  ferrite nanoparticles



of vibrations, out of which only five first-order modes such as  $1A_{1g}$ ,  $1E_g$ , and  $3T_{2g}$  are Raman active [32] (Fig. 3). Figure 4a shows the Raman spectra of  $\text{MnFe}_2\text{O}_4$ . It is seen that there are six obvious first-order Raman modes noticed at  $T_{2g} \sim 220.6$ ,  $E_g \sim 277$ ,  $T_{2g} \sim 370.9$ ,  $T_{2g} \sim 507.4$ ,  $A_{1g} \sim 593$ , and  $A_{1g} \sim 638.7 \text{ cm}^{-1}$ , respectively. Figure 4f shows the Raman spectra of  $\text{ZnFe}_2\text{O}_4$ . It is seen that there are four obvious first-order Raman modes noticed at  $T_{2g} \sim 174.9$ ,  $T_{2g} \sim 340.3$ ,  $E_g \sim 491.0$ ,  $A_{1g} \sim 652.7$ , and  $A_{1g} \sim 688.6$ . These bands are in agreement with the previously reported data of  $\text{MnFe}_2\text{O}_4$  and  $\text{ZnFe}_2\text{O}_4$  nanoparticles [33]. Meanwhile, it is noticed that the position of Raman peaks of  $\text{ZnFe}_2\text{O}_4$  is different from that of  $\text{MnFe}_2\text{O}_4$ . A

similar kind of difference in Raman spectra of spinel ferrites is reported in literature [33, 34]. The bulk  $\text{ZnFe}_2\text{O}_4$  is a completely normal ferrite [6], whereas  $\text{MnFe}_2\text{O}_4$  is 80 % normal [2]. In addition to that, the Mn atoms are having the possibility of  $\text{Mn}^{2+}$  and  $\text{Mn}^{3+}$  ionic states in octahedral sites as discussed earlier in PXRD analysis. The observed difference in position of Raman vibrational modes of  $\text{ZnFe}_2\text{O}_4$  and  $\text{MnFe}_2\text{O}_4$  is attributed to different kinds of cation distribution, ionic state, and size effect [35]. Among all the observed modes, the modes above  $600 \text{ cm}^{-1}$  corresponding to the tetrahedral sub-lattices and below refer to octahedral sub-lattices. It is noticed that the mode corresponds to the tetrahedral site ( $A_{1g}$ ), splits into (minimum

two and maximum three) different energy levels due to the mass difference between the three ions ( $\text{Mn}^{2+}$ ,  $\text{Zn}^{2+}$ , and  $\text{Fe}^{3+}$ ) present in the tetrahedral sites, and further confirms the presence of  $\text{Fe}^{3+}$  in tetrahedral sites of  $\text{ZnFe}_2\text{O}_4$ . Moreover, the obtained Raman spectra of all the samples confirm the spinel structure of  $\text{Mn}_{1-x}\text{Zn}_x\text{Fe}_2\text{O}_4$  nanoparticles and rule out the existence of the secondary phase  $\alpha\text{-Fe}_2\text{O}_3$ , which usually gives strong bands at  $\sim 240$  and  $\sim 300\text{ cm}^{-1}$ .

### 3.3 Surface Morphological Analysis

The surface morphological information of all the samples was observed using the FE-SEM images. The FE-SEM images of all the samples are shown in Fig. 3. It can be seen that the prepared  $\text{Mn}_{1-x}\text{Zn}_x\text{Fe}_2\text{O}_4$  ferrite nanoparticles are roughly spherical in shape and admit the agglomerated coalescence behavior of the particles. Further we have noticed that the substitution of  $\text{Zn}^{2+}$  does not have a huge impact on the surface morphology of  $\text{Mn}_{1-x}\text{Zn}_x\text{Fe}_2\text{O}_4$  nanoparticles.

### 3.4 Elemental Compositional Analyses

The elemental compositional analyses of  $\text{Mn}_{1-x}\text{Zn}_x\text{Fe}_2\text{O}_4$  nanoparticles are carried out by using EDS and the obtained spectra of all the samples are depicted in Fig. 4. From the EDS results of  $\text{MnFe}_2\text{O}_4$  the peaks corresponding to the elements Mn, Fe and O are observed and have been assigned, whereas the substitution of Zn atom is confirmed by the emergence of a strong peak in  $\sim 1\text{ keV}$ . No other traceable impurities are identified within the resolution limit of EDS.

### 3.5 Magnetic Study

In order to study the magnetic properties, we have measured the field-dependent magnetization of  $\text{Mn}_{1-x}\text{Zn}_x\text{Fe}_2\text{O}_4$  ( $x = 0.0, 0.2, 0.4, 0.6, 0.8$ , and  $1.0$ ) ferrite nanoparticles at 300 and 20 K up to 1.5 T. The magnetic hysteresis curves measured at 300 K are shown in Fig. 5 for all the samples. It is noticed that magnetization of all samples are unsaturated and both the coercivity and the remanence are negligible, which indicates the superparamagnetic nature of  $\text{Mn}_{1-x}\text{Zn}_x\text{Fe}_2\text{O}_4$ . The thermal fluctuation causes the spins to flip between the easy magnetization axes, which allow increase in saturation magnetization and near zero coercivity. The measured values of saturation magnetization are given in Table 2. It is observed that for pure  $\text{MnFe}_2\text{O}_4$  with the crystallite size of 8.5 nm, a  $M_s$  of  $31.12\text{ emu g}^{-1}$  is obtained, while the reported value in the literature for bulk  $\text{MnFe}_2\text{O}_4$  is about  $80\text{ emu g}^{-1}$  [36]. The reduction in magnetization is attributed to the surface effect of the smaller-size magnetic particles. This surface effect can be explained by postulating the existence of a magnetic dead layer due to the spin disorder at the surface [37–39]. It

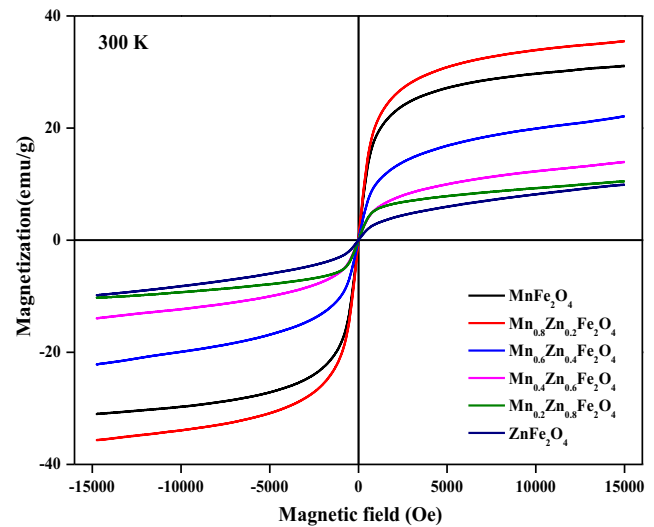


**Fig. 5** Hysteresis curves of  $\text{Mn}_{1-x}\text{Zn}_x\text{Fe}_2\text{O}_4$  ferrite nanoparticles at 300 K

is observed that the  $M_s$  value is found to increase up to  $x = 0.2$  and then decrease. The initial increase of saturation magnetization of  $\text{Mn}_{0.8}\text{Zn}_{0.2}\text{Fe}_2\text{O}_4$  is understood in terms of the super exchange interactions and distribution of magnetic and non-magnetic ions in the tetrahedral and octahedral sites using Neel's sub-lattice model [40, 41]. According to that, the spinel structure has three types of magnetic interaction between tetrahedral (A) and octahedral (B) interstitial sites, such as A–A, B–B, and A–B. The strength of magnetic interactions between A and B site ions depends on the distances between the ions and the oxygen ion and the angle between the three ions. In case of A–A and B–B interactions, the angles are very small and the distance between the metal ions and the oxygen ions is very large. In contrast, the angle between A–O–B is high compared with A–A and B–B interactions. Therefore, the interaction between moments of the A and B sites is strongest. The  $\text{ZnFe}_2\text{O}_4$  in bulk form has a normal spinel structure with an antiferromagnetic nature, in which all the  $\text{Zn}^{2+}$  ( $0\ \mu_B$ ) cations are located in A sites due to their strong preference for A sites and all  $\text{Fe}^{3+}$  ( $5\ \mu_B$ ) cations are located in B sites with antiparallel magnetic moments. Therefore, the substitution of non-magnetic  $\text{Zn}^{2+}$  ions initially occupying preferred A sites results in the reduction of the A site magnetic moment. According to Neel, the magnetization is the result of the difference between the magnetic moments of the B and A sites; the saturation magnetization of  $\text{Mn}_{0.8}\text{Zn}_{0.2}\text{Fe}_2\text{O}_4$  increases. We have observed that for further substitution of  $\text{Zn}^{2+}$  ( $x \leq 0.4$ ), the magnetization decreases gradually. Since the substitution weakens the moment of the A site, subsequently, the exchange interaction between the B and A sites decreases and hence magnetization decreases [42].

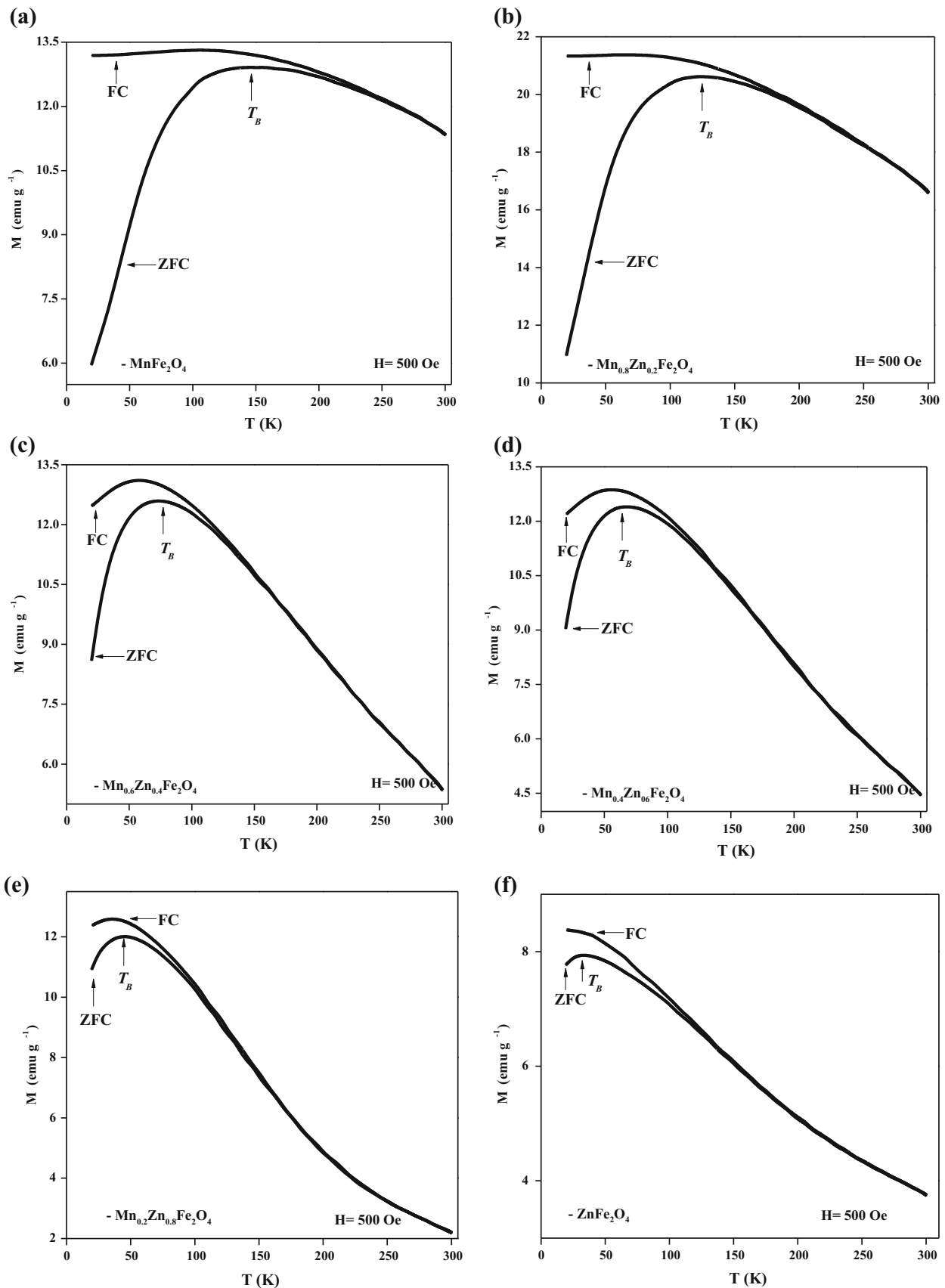


**Fig. 6** ZFC and FC curves of  $\text{Mn}_{1-x}\text{Zn}_x\text{Fe}_2\text{O}_4$  ferrite nanoparticles measured under an applied magnetic field of 500 Oe



### 3.6 ZFC-FC Measurement

To examine the superparamagnetic nature of  $\text{Mn}_{1-x}\text{Zn}_x\text{Fe}_2\text{O}_4$  ferrite nanoparticles, the zero-field-cooled (ZFC)–field-cooled (FC) magnetization profiles have been done from 20 to 300 K. In ZFC mode, the samples cooled from 300 K down to 20 K in the absence of a magnetic field. At 20 K, a measuring field of 500 Oe was applied and ZFC measurements were made from 20 to 300 K. In FC mode, the samples cooled from 300 to 20 K in the presence of 500 Oe external magnetic field and measurement was carried out from 20 to 300 K with the same field in the warming cycle. Figure 6a–f depicts the ZFC and FC magnetization curves of  $\text{Mn}_{1-x}\text{Zn}_x\text{Fe}_2\text{O}_4$  ferrite nanoparticles. The data reveal irreversibility between the ZFC and FC curves. Furthermore, it is noticed that the ZFC magnetization curves exhibit a broad maximum centered at a certain temperature. By contrast, the FC magnetization gradually increases with decreasing temperature from 300 K and becomes almost constant below a certain temperature. When  $\text{Mn}_{1-x}\text{Zn}_x\text{Fe}_2\text{O}_4$  nanoparticles are cooled to a low temperature (20 K) without an external applied magnetic field, the net magnetic moments in each single-domain  $\text{Mn}_{1-x}\text{Zn}_x\text{Fe}_2\text{O}_4$  nanoparticle align along their easy axis to attain a local minimum of potential energy. To prevent the magnetization direction from switching away from the easy axis, the magnetic anisotropy of nanoparticles behaves as an energy barrier. When temperature increases from 20 K, the magnetic anisotropy is gradually overcome and the directions of magnetization of thermally activated nanoparticles start to align to the external magnetic field. Therefore, the total magnetization increases initially with rising temperature. When a certain temperature is reached, the magnetic anisotropy energy barrier overcomes by thermal activation and the magnetization direction of the nanoparticle starts to fluctuate, leading to a superparamagnetic state [43]. The temperature at which thermal energy breaks magnetic anisotropy energy and shows a broad maximum in ZFC curves is called blocking temperature  $T_B$  [44]. The blocking temperature is a characteristic of single-domain magnetic nanoparticles. The blocking temperature of a single-domain particle is described by the relation

$$T_B = KV/25k_B, \quad (3)$$

where  $K$  is the magnetocrystalline anisotropy,  $V$  is the volume of the nanoparticle, and  $k_B$  is the Boltzmann constant. The obtained values of blocking temperature of  $\text{Mn}_{1-x}\text{Zn}_x\text{Fe}_2\text{O}_4$  nanoparticles are given in Table 2. It can be observed from Table 2 that the  $T_B$  is shifted towards the low temperatures with the substitution of  $\text{Zn}^{2+}$ . The weak magnetocrystalline anisotropy of  $\text{Zn}^{2+}$  ion causes the decrease in the blocking temperature of  $\text{Mn}_{1-x}\text{Zn}_x\text{Fe}_2\text{O}_4$  [45]. Below  $T_B$ , the superparamagnetic particles cannot

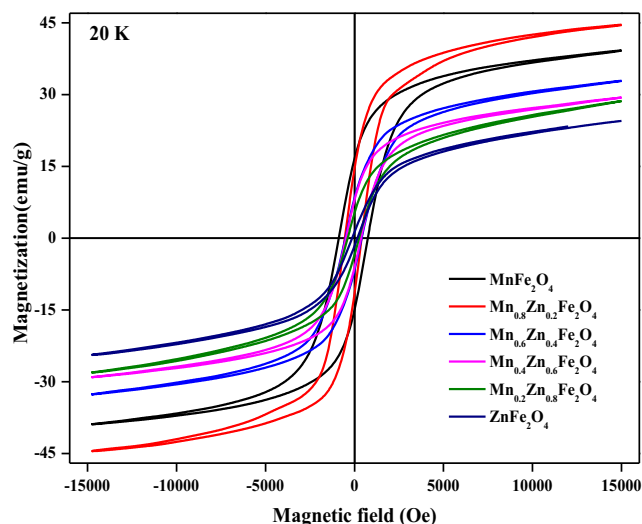


**Fig. 7** Magnetic hysteresis loops of  $\text{Mn}_{1-x}\text{Zn}_x\text{Fe}_2\text{O}_4$  ferrite nanoparticles measured at 20 K

rotate freely since they freeze in random orientations of spins resulting in higher coercive fields at low temperature. To elucidate that, the magnetic hysteresis curves measured at 20 K are shown in Fig. 7 for all the samples. We have noticed that all samples show hysteresis behavior with coercivity. The obtained values of the coercivity ( $H_c$ ), the remanence ( $M_r$ ), and the saturation magnetization ( $M_s$ ) are given in Table 2. As expected at 20 K,  $\text{Mn}_{1-x}\text{Zn}_x\text{Fe}_2\text{O}_4$  ferrite nanoparticles exhibit coercivity. It is seen that pure  $\text{MnFe}_2\text{O}_4$  has a coercivity of 810 Oe. The substitution of  $\text{Zn}^{2+}$  decreases the coercivity of the samples. The variation in coercivity can be attributed to the reduction of domain wall energy caused by the weak magnetocrystalline anisotropy of the  $\text{Zn}^{2+}$  ion [45]. Moreover, it is observed that at 20 K the saturation magnetization values of all the samples are higher than those at 300 K. For pure  $\text{MnFe}_2\text{O}_4$ , a  $M_s$  value of  $39.16 \text{ emu g}^{-1}$  is found at 20 K. The increase in saturation magnetization compared with 300 K is attributed to the decrease of the thermal fluctuation and surface spin disorder at the surface of the nanoparticles [46].

### 4 Conclusion

In summary, the Zn content has significant influence on the structural and magnetic properties of  $\text{Mn}_{1-x}\text{Zn}_x\text{Fe}_2\text{O}_4$  ( $x = 0-1$ ) ferrite nanoparticles prepared using the novel combustion method. The PXRD analysis shows the single-phase nature of  $\text{Mn}_{1-x}\text{Zn}_x\text{Fe}_2\text{O}_4$  ferrites and the crystallite size increases for Zn substitution. Raman spectra analysis further confirms the formation of the spinel structure. The FE-SEM images show the surface morphology and EDS confirm the presence of constitution elements.

Magnetic measurements showed superparamagnetic behavior and a strong compositional dependence of the saturation magnetization that differs from studies in bulk phases, with the highest value obtained for  $\text{Mn}_{0.8}\text{Zn}_{0.2}\text{Fe}_2\text{O}_4$  at 300 and 20 K. The magnetization process has been explained based on the crystallite size, cation distribution, Neel's sub-lattice model, and exchange interaction between the tetrahedral and octahedral sites.

**Acknowledgments** The authors thank the Central Instrumentation Facility, Pondicherry University, and DST-FIST, Government of India, for funding the facilities utilized in the present work and the Center for Nano Science and Technology for providing XRD measurement. C.M. thanks UGC, New Delhi, India, for the financial assistance in the form of the Rajiv Gandhi National Fellowship (RGNF).

## References

- Standley, K.J.: Oxide Magnetic Materials. Oxford University Press (1972)
- Dionne, G.F.: Magnetic Oxides. Springer (2009)
- Goldman, A.: Modern Ferrite Technology. Springer Science & Business Media (2006)
- Corot, C., Robert, P., Idée, J.-M., Port, M.: Recent advances in iron oxide nanocrystal technology for medical imaging. *Adv Drug Deliv Rev* **58**, 1471–1504 (2006)
- Valenzuela, R.: Novel applications of ferrites. *Physiother Res Int*, 2012 (2012)
- Cullity, B.D., Graham, C.D.: Introduction to Magnetic Materials. Wiley (2011)
- Snoek, J.L.: New Developments in Ferromagnetic Materials. Elsevier Publishing Company (1949)
- Agrafiotis, C., Zaspalis, V.: Self-propagating high-temperature synthesis of MnZn-ferrites for inductor applications. *J. Magn. Magn. Mater.* **283**, 364–374 (2004)
- Arshak, K., Ajina, A., Egan, D.: Development of screen-printed polymer thick film planner transformer using Mn–Zn ferrite as core material. *Microelectron. J.* **32**, 113–116 (2001)
- Waqas, H., Qureshi, A.: Influence of pH on nanosized Mn–Zn ferrite synthesized by sol–gel auto combustion process. *J. Therm. Anal. Calorim.* **98**, 355–360 (2009)
- Masuda, Y., Akiyama, T., Kitaoka, M., Otobe, S., Takei, H.: Development of new ferrite material for deflection yoke core. *SID Symposium Digest of Technical Papers* **29**, 343–346 (1998)
- Keluskar, S., Tangsali, R., Naik, G., Budkuley, J.: High permeability of low loss Mn–Zn ferrite obtained by sintering nanoparticle Mn–Zn ferrite. *J. Magn. Magn. Mater.* **305**, 296–303 (2006)
- Sugimoto, M.: The past, present, and future of ferrites. *J. Am. Ceram. Soc.* **82**, 269–280 (1999)
- Zhang, Z., Xu, L., Liu, C.: Preparation and characterization of composite magnetic photocatalyst  $\text{Mn}_x\text{Zn}_{1-x}\text{Fe}_2\text{O}_4/\beta\text{-Bi}_2\text{O}_3$ . *RSC Advances*. **5**, 79997–80004 (2015)
- Kondo, T., Mori, K., Hachisu, M., Yamazaki, T., Okamoto, D., Watanabe, M., Gonda, K., Tada, H., Hamada, Y., Takano, M., Ohuchi, N., Ichiyangi, Y.: Alternating current magnetic susceptibility and heat dissipation by  $\text{Mn}_{1-x}\text{Zn}_x\text{Fe}_2\text{O}_4$  nanoparticles for hyperthermia treatment. *J. Appl. Phys.* **117**, 17D157 (2015)
- Zhuang, L., Zhang, W., Zhao, Y., Li, D., Wu, W., Shen, H.: Temperature sensitive ferrofluid composed of  $\text{Mn}_{1-x}\text{Zn}_x\text{Fe}_2\text{O}_4$  nanoparticles prepared by a modified hydrothermal process. *Powder Technol.* **217**, 46–49 (2012)
- Ahmed, M.A., Okasha, N., El-Dek, S.I.: Preparation and characterization of nanometric Mn ferrite via different methods. *Nanotechnology* **19**, 065603 (2008)
- Azadmanjiri, J.: Preparation of Mn–Zn ferrite nanoparticles from chemical sol–gel combustion method and the magnetic properties after sintering. *J. Non-Cryst. Solids.* **353**, 4170–4173 (2007)
- Rath, C., Anand, S., Das, R., Sahu, K., Kulkarni, S., Date, S., Mishra, N.: Dependence on cation distribution of particle size, lattice parameter, and magnetic properties in nanosize Mn–Zn ferrite. *J. Appl. Phys.* **91**, 2211 (2002)
- Pemartin, K., Solans, C., Alvarez-Quintana, J., Sanchez-Dominguez, M.: Synthesis of Mn–Zn ferrite nanoparticles by the oil-in-water microemulsion reaction method. *Colloids Surf. A Physicochem. Eng. Asp.* **451**, 161–171 (2014)
- Seyyed Ebrahimi, S.A., Masoudpanah, S.M.: Effects of pH and citric acid content on the structure and magnetic properties of MnZn ferrite nanoparticles synthesized by a sol–gel autocombustion method. *J. Magn. Magn. Mater.* **357**, 77–81 (2014)
- Shultz, M., Allsbrook, M., Carpenter, E.: Control of the cation occupancies of MnZn ferrite synthesized via reverse micelles. *J. Appl. Phys.* **101**, 09M518 (2007)
- Arulmurugan, R., Jeyadevan, B., Vaidyanathan, G., Sendhilnathan, S.: Effect of zinc substitution on Co–Zn and Mn–Zn ferrite nanoparticles prepared by co-precipitation. *J. Magn. Magn. Mater.* **288**, 470–477 (2005)
- Cullity, B.D., Stock, S.R.: Elements of X-ray Diffraction, 3rd edn. Prentice-Hall, New York (2001)
- Aslibeiki, B.: Nanostructural, magnetic and electrical properties of Ag doped Mn-ferrite nanoparticles. *Curr. Appl. Phys.* **14**, 1659–1664 (2014)
- Gul, I.H., Ahmed, W., Maqsood, A.: Electrical and magnetic characterization of nanocrystalline Ni–Zn ferrite synthesis by co-precipitation route. *J. Magn. Magn. Mater.* **320**, 270–275 (2008)
- Syue, M.-R., Wei, F.-J., Chou, C.-S., Fu, C.-M.: Magnetic and electrical properties of Mn–Zn ferrites synthesized by combustion method without subsequent heat treatments. *J. Appl. Phys.* **109**, 07A324 (2011)
- Tang, Z.X., Chen, J.P., Sorensen, C.M., Klabunde, K.J., Hadjipanayis, G.C., Tang, et al.: Reply. *Phys. Rev. Lett.* **68**, 3114–3114 (1992)
- Gopalan, E.V., Al-Omari, I., Malini, K., Joy, P., Kumar, D.S., Yoshida, Y., Anantharaman, M.: Impact of zinc substitution on the structural and magnetic properties of chemically derived nanosized manganese zinc mixed ferrites. *J. Magn. Magn. Mater.* **321**, 1092–1099 (2009)
- Shannon, R., Gurneman, P., Chenavas, J.: Effect of octahedral distortion on mean  $\text{Mn}^{3+}$ -O distances. *Mineralogical Soc Amer* 1130 17th St Nw Suite **330**, 714–716 (1975). DC 20036
- Shebanova, O.N., Lazor, P.: Raman spectroscopic study of magnetite ( $\text{FeFe}_2\text{O}_4$ ): a new assignment for the vibrational spectrum. *J. Solid State Chem.* **174**, 424–430 (2003)
- White, W.B., DeAngelis, B.A.: Interpretation of the vibrational spectra of spinels. *Spectrochim. Acta A: Mol. Spectrosc.* **23**, 985–995 (1967)
- Diodati, S., Pandolfo, L., Caneschi, A., Gialanella, S., Gross, S.: Green and low temperature synthesis of nanocrystalline transition metal ferrites by simple wet chemistry routes. *Nano Res.* **7**, 1027–1042 (2014)
- Xu, Y., Sherwood, J., Qin, Y., Holler, R.A., Bao, Y.: A general approach to the synthesis and detailed characterization of magnetic ferrite nanocubes. *Nanoscale* **7**, 12641–12649 (2015)
- Sekulić, D., Lazarević, Z., Jovalekić, Č., Rečnik, A., Romčević, M., Hadžić, B., Romčević, N.: The comparative study of the

- structural and the electrical properties of the nano spinel ferrites prepared by the soft mehanochemical synthesis. *Sci. Sinter.* **46**, 235–245 (2014)
36. Tang, Z.X., Sorensen, C.M., Klabunde, K.J., Hadjipanayis, G.C.: Size-dependent Curie temperature in nanoscale  $\text{MnFe}_2\text{O}_4$  particles. *Phys. Rev. Lett.* **67**, 3602–3605 (1991)
  37. Zheng, M., Wu, X.C., Zou, B.S., Wang, Y.J.: Magnetic properties of nanosized  $\text{MnFe}_2\text{O}_4$  particles. *J. Magn. Magn. Mater.* **183**, 152–156 (1998)
  38. Chen, J., Sorensen, C., Klabunde, K., Hadjipanayis, G., Devlin, E., Kostikas, A.: Size-dependent magnetic properties of  $\text{MnFe}_2\text{O}_4$  fine particles synthesized by coprecipitation. *Phys. Rev. B* **54**, 9288 (1996)
  39. Kodama, R.H., Berkowitz, A.E., McNiff, J.E.J., Foner, S.: Surface spin disorder in  $\text{NiFe}_2\text{O}_4$  nanoparticles. *Phys. Rev. Lett.* **77**, 394–397 (1996)
  40. Neel, L.: Magnetic properties of ferrites: ferrimagnetism and antiferromagnetism. *Ann. Phys.* **3**, 137–198 (1948)
  41. Néel, L.: Antiferromagnetism and ferrimagnetism. *Proc. Phys. Soc. London, Sect. A* **65**, 869 (1952)
  42. Smith, J., Wijn, H.P.J.: *Ferrites*. Wiley, New York (1959)
  43. Lu, A.-H., Salabas, E.L., Schüth, F.: Magnetic nanoparticles: synthesis, protection, functionalization, and application. *Angew. Chem. Int. Ed.* **46**, 1222–1244 (2007)
  44. Liu, C., Zou, B., Rondinone, A.J., Zhang, Z.J.: Reverse micelle synthesis and characterization of superparamagnetic  $\text{MnFe}_2\text{O}_4$  spinel ferrite nanocrystallites. *J. Phys. Chem. B* **104**, 1141–1145 (2000)
  45. Ali, M.B., El Maalam, K., El Moussaoui, H., Mounkachi, O., Hamedoun, M., Masrour, R., Hlil, E., Benyoussef, A.: Effect of zinc concentration on the structural and magnetic properties of mixed Co–Zn ferrites nanoparticles synthesized by sol/gel method. *J. Magn. Magn. Mater.* **398**, 20–25 (2016)
  46. Murugesan, C., Chandrasekaran, G.: Impact of  $\text{gd}^{3+}$  substitution on the structural, magnetic and electrical properties of cobalt ferrite nanoparticles. *RSC Adv.* **5**, 73714–73725 (2015)